THE JOURNAL OF PHYSICAL CHEMISTRY B
A JOURNAL OF THE AMERICAN CHEMICAL SOCIETY

pubs.acs.org/JPCB

Article

Adhesive Dynamics Simulations of Highly Polyvalent DNA Motors

Aaron T. Blanchard,* Selma Piranej, Victor Pan, and Khalid Salaita*

Cite This: J. Phys. Chem. B 2022, 126, 7495−7509

Read Online

ACCESS | Metrics & More | Article Recommendations | Supporting Information

ABSTRACT: Molecular motors, such as myosin and kinesin, perform diverse tasks ranging from vesical transport to bulk muscle contraction. Synthetic molecular motors may eventually be harnessed to perform similar tasks in versatile synthetic systems. The most promising type of synthetic molecular motor, the DNA walker, can undergo processive motion but generally exhibits low speeds and virtually no capacity for force generation. However, we recently showed that highly polyvalent DNA motors (HPDMs) can rival biological motors by translocating at micrometer per minute speeds and generating 100+ pN of force. Accordingly, DNA nanotechnology-based designs may hold promise for the creation of synthetic, force-generating nanomotors. However, the dependencies of HPDM speed and force on tunable design parameters are poorly understood and difficult to characterize experimentally. To overcome this challenge, we present RoloSim, an adhesive dynamics software package for fine-grained simulations of HPDM translocation. RoloSim uses biophysical models for DNA duplex formation and dissociation kinetics to explicitly model tens of thousands of molecular scale interactions. These molecular interactions are then used to calculate the nano- and microscale motions of the motor. We use RoloSim to uncover how motor force and speed scale with several tunable motor properties such as motor size and DNA duplex length. Our results support our previously defined hypothesis that force scales linearly with polyvalency. We also demonstrate that HPDMs can be steered with external force, and we provide design parameters for novel HPDM-based molecular sensor and nanomachine designs.

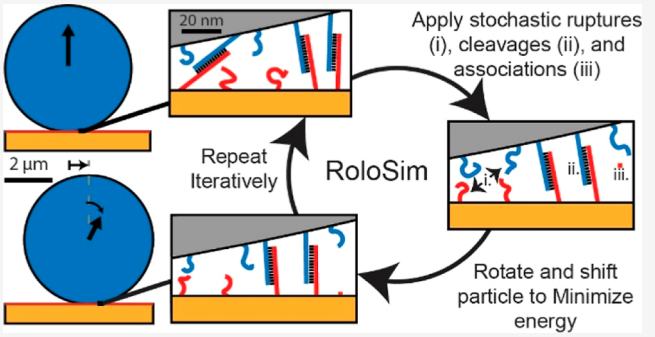

INTRODUCTION

Molecular motors such as myosin and kinesin[1,2] consume ATP to generate forces on the order of 1−10 pN. Through sophisticated regulation and coordination, these motors power countless biological tasks such as cargo transport, tissue formation, cell migration, and muscle contraction. A number of exciting applications—from molecular robotics to synthetic muscles and chemical sensing—may become available if one could create molecular motors that mimic the basic functions of biological motors to generate pN forces. Thus, the de novo design of synthetic molecular motors is a pressing challenge. Addressing this challenge may also be useful in that it could reveal the fundamental properties of biological motors and enable the development of versatile nanomachines.[3]

Some of the most promising synthetic analogues of biological molecular motors are DNA-based walkers.[4−26] Unlike cytoskeletal walkers, DNA walkers do not translocate along filaments via directional ATP-fuel conformational changes. Rather, DNA walkers are generally engineered to translocate along linear or planar tracks through DNA based "feet" that iteratively hybridize to and destroy track-bound oligonucleotide "fuel" strands. Foot-fuel hybridization pulls the motor along the track, while fuel destruction frees the foot to bind to new fuel and prevents backward translocation. Early examples of DNA-based motors were nanoscale walkers with 2−4 feet that degraded DNA or RNA fuel via toehold-mediated strand displacement or catalytic DNAzyme-based feet.[11,13,27−29] Such motors can perform diverse chemical tasks such as sequential chemical synthesis,[9] cargo sorting,[22] and molecular computing[20] but exhibit no capacity for force-generation and are orders of magnitude slower than biological motors. More recently, higher polyvalent motors with hundreds or thousands of feet scaffolded onto micro-particles,[17,30] nanoparticles,[25] or DNA origami rods[26] were shown to travel at velocities within an order-of-magnitude of the velocities of biological motors. Microparticle DNA motors were found to generate 100+ pN forces[30] via a mechanism termed autochemophoresis (where "chemophoresis" describes transport up an adhesion gradient[31] and the prefix "auto-" reflects the self-propagated nature[32] of the gradient). These highly polyvalent DNA motors (HPDMs) have DNA-based feet that hybridize to RNA strands, forming "tethers" attached to a planar track (Figure 1). The HPDMs' aqueous

Received: March 18, 2022
Revised: June 25, 2022
Published: September 22, 2022

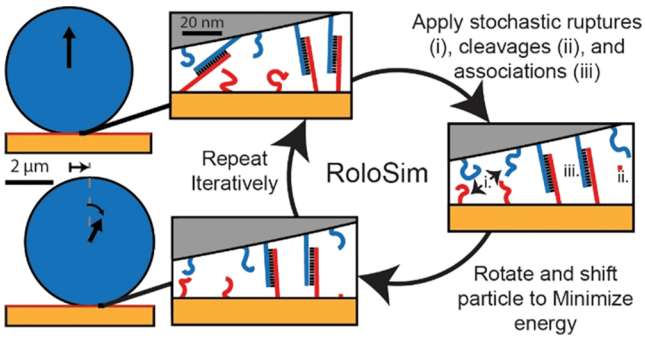

Figure 1. Schematic depiction of the iterative RoloSim simulation method.

environment contains the enzyme ribonuclease H (RNase H), which rapidly and selectively binds to and covalently cleaves the RNA in the RNA-DNA duplexes beneath the HPDM. The fast catalytic rate of RNase H enables fast translocation, while the high polyvalency of the motor prevents dissociation of the HPDM from the planar track.[17]

The ability of HPDMs to generate forces on the order of 100 pN illustrates the potential of tethers to act as self-coordinating molecular motor units. Broadly speaking, HPDMs demonstrate the potential of motors that operate through the burnt bridge ratchet (BBR) mechanism to generate pN-scale force. Numerous examples of BBR translocation have been discovered in biological systems, including in bacterial plasmid replication,[33] influenza infection,[34,35] mammalian cell migration,[36] and enzymatic filament degradation.[37,38] The diversity of these examples and the simplicity of components required for BBR to occur make it likely that the BBR mechanism has independently evolved countless times across many domains of life.[39] BBR motors are also increasingly used in fully synthetic applications.[40] A detailed understanding of the fundamental characteristics of BBR-mediated force generation is thus of fundamental biological and engineering significance, with HPDMs being the most versatile model system currently available.

Despite the customizability and versatility offered by DNA nanotechnology, there are still many limits to experimental characterizations of HPDM translocation. For example, while HPDM dynamic properties such as velocity can be resolved via particle tracking experiments,[17,25,26,30] the dynamics of individual molecular-level foot−fuel interactions cannot be resolved with current methods. Mean field theory-based modeling suggests that motor force scales with average polyvalency (the number of tethers bound to an HPDM). Testing this prediction experimentally is challenging because polyvalency cannot currently be measured. In addition, current methods for quantitatively measuring HPDM force require an integrated computational analysis of hundreds of HPDMs translocating under a large number (∼15) of independent conditions.[30] Coupled with limits associated with small-but-meaningful variability between experiments, current methods are challenging to implement for scaling studies of the relationships between HPDM force and tunable properties such as HPDM size and the surface density of feet and fuel molecules.

An emerging technique to complement BBR studies is the use of coarse-grained simulations that explicitly model interactions between feet and fuel molecules, and the subsequent effects of these interactions on motor transport.[33,41−48] These simulations help reveal how molecular-level interactions produce motor-level dynamic behavior and aid in hypothesis generation. However, such simulations have typically focused on small motors with polyvalency on the order of a few tethers. In recent work, Hu et al. simulated BBR motors with hundreds of tethers simultaneously[41,49] but did not investigate motor force or account for motor rolling, which is fundamental to HPDM translocation.

In this work, we present simulations of HPDMs with hundreds or thousands of tethers. Our software package, which we term RoloSim, leverages an adhesive dynamics framework to simulate HPDM motion with molecular-level details on experimentally relevant timescales. We use RoloSim to investigate the effects of various experimentally tunable parameters on HPDM force and velocity, finding important effects of HPDM geometry, RNase H concentration, foot/fuel length, and surface density. Throughout this work, we fit our simulation results to simple scaling laws and successfully apply our scaling laws to accurately predict the average velocity of a nanoparticle-based HPDM.[25] We also use RoloSim to predict that HPDMs can be directed with an externally applied force field and provide experimental validation of this prediction.

BACKGROUND THEORY: ADHESIVE DYNAMICS

Here, we present RoloSim, a simulation package used to simulate HPDM translocation. RoloSim can be described as a type of adhesive dynamics[50] (AD) simulation. AD has been used to simulate the adhesive and/or transport properties of nanoscale biological adhesion structures[51,52] and whole cells[53] interacting with external objects through specific receptor−ligand interactions. AD-like simulations have also been used extensively to study the transport properties of BBR systems such as multi-legged burnt bridge molecular motors,[43,45−47,54−57] influenza particles,[35,58] and the bacterial partition system.[41,49]

In AD, a "body" (such as a cell, plasma membrane, a colloidal particle, or an infinitesimal point) is decorated with multiple adhesive molecules. The body is close to a surface that itself is decorated with a second type of adhesive molecule. We can call these two types of molecules B (adhesive molecules on the body) and S (adhesive molecules on the surface). The two types of molecules interact with each other to form tethers (SB). Each tether then acts as a spring that exerts force on the body such that the position and orientation of the body are controlled by the set of tethers that are bound to it.

Generally, AD is the recursive iteration of two steps (Figure 1): the simulation method is an iterative process which alternates between (1) calculating distance-dependent rate constants and stochastically applying associations, cleavages, and ruptures, and (2) minimizing the system's potential energy via rigid body motion.

Apply Stochastic Changes. Tethers are formed and degraded using the kinetic Monte Carlo method with kinetic rate constants k_{on} and k_{off}. In the kinetic Monte Carlo method, the probability, p, of a single event with kinetic rate constant k occurring within a timestep of duration Δt is equal to $p = 1-\exp(-k\Delta t)$. Generally, k_{on} is negatively correlated with the distance, d, between S and B such that pairs that are closer together are more likely to associate than pairs that are farther away. Similarly, k_{off} may also depend on the tether's end-to-end extension, r, to reflect force-induced tether rupture. In the case of burnt-bridge motor modeling, k_{off} has an extension-independent, constant component that reflects irreversible

https://doi.org/10.1021/acs.jpcb.2c01897
J. Phys. Chem. B 2022, 126, 7495−7509

"consumption" of the *S* species. Following consumption, these "burnt" molecules can no longer form new tethers (although in some cases, burnt molecules can undergo time-dependent regeneration[41,49]).

Calculate New Energetic Minimum of the System. The position and orientation of the body (and, in some cases, deformation of the body and surface) are then calculated using energy minimization methods. Energy, *E*, can be broken up into two terms

$$E = E_{sys} + \sum_{i=1}^{N} E_{teth,i} \tag{1}$$

where $E_{teth,i}$ represents the mechanical strain energy of the i^{th} tether, N is the number of tethers, and E_{sys} encompasses all other energetic terms of the system that can include (1) gravity, (2) body-surface repulsion, (3) externally applied biasing forces, and (4) strain energy terms that govern deformation of the body and/or surface. In some cases, random thermal energy terms may be added to reflect the tethered Brownian motion of the body. The energetic minimum of the system may have an analytic solution (often true when tethers are modeled as linear springs), but numerical methods (e.g., gradient descent) can be used when an analytical form is not available. RoloSim adheres to this AD framework. A RoloSim user guide, with accompanying Figures S1−S6, is presented in the Supporting Information.

METHODS

The development and execution of RoloSim was performed in MATLAB 2019b on a laptop computer with 32 GB of RAM and an Intel Xeon E−2276 M CPU processor. High throughput simulations were performed on the Partnership for an Advanced Computing Environment (PACE) computer cluster at the Georgia Institute of Technology. Each iteration on the Duke compute cluster was run on a single core with 8 GB of RAM and a wall time of 7 days. Figures were prepared using Adobe Illustrator CC 2019. Experiments were performed as described previously;[30] on a Nikon Eclipse Ti Microscope at standard buffer conditions (0.5x RNase H buffer with 144 nM RNase H in the presence of 10% formamide v/v, 10 μM DTT, and 0.75% triton-X w/v). DNA guide strands were conjugated to silica microspheres via click chemistry, while RNA fuel strands were conjugated to the gold-coated glass surface via thiol−gold binding.

RESULTS

Engineering Objectives. We had four specific goals that we sought to use RoloSim to accomplish, which are discussed in greater detail in Note S1 (accompanied by Figure S7). In brief, our first goal was to use RoloSim to understand general scaling properties of HPDM force and velocity with control parameters such as HPDM diameter, tether length, and the surface density of fuel and foot strands. A second goal revolves around the potential molecular sensing capabilities of HPDMs, which entails understanding how to decrease HPDM force while retaining large HPDM size. Our third goal was to understand whether HPDM force generation could be preserved using nanoscale motors. This goal centered on the exploration of rod-shaped HPDMs, which can have similar HPDM-surface contact areas but vastly reduced volumes. Finally, our fourth goal involved HPDM control by testing whether externally applied bias forces could be used to steer HPDM translocation.

Model Description. In RoloSim, DNA strands are randomly scaffolded on a microsphere at the previously measured density of 91 000 strands/μm^2 and RNA fuel strands are randomly patterned on an underlying planar surface (which we call the "substrate") at a density of 50 000 strands/μm^2. Specific hybridization interactions between the particle-bound DNA feet and the surface-bound RNA fuel form "molecular tethers". Each tether exerts an extension (r)-dependent force on the microsphere. Every single strand is explicitly modeled, such that the simulated HPDM acts as a "virtual twin" of a real HPDM. RoloSim allows for the simulation of spherical particles, as well as more complex geometries including dimers and trimers of spheres, rods with spherical caps, and polygonal prisms (not shown). RoloSim faithfully reproduces many characteristics of HPDM motion that we have observed experimentally. A 30 min simulation with a 30 ms timestep can be completed in ∼24 h. We generally run hundreds of RoloSim simulations in parallel using a computing cluster. A more detailed description of RoloSim is offered in the User Guide in the Supporting Information.

Energy Minimization. At each timestep, the position (encoded by the vector $\boldsymbol{P} = [P_x, P_y, P_z]^T$, which describes the particle's geometric centroid) and orientation of the HPDM is adjusted to minimize *E*. The coordinates of all DNA strands are rigidly linked to the HPDM's surface, such that any rotation or translation of the particle is also propagated to the DNA strands' coordinates. The simulation operates in an $x-y-z$ Cartesian coordinate system where the z-direction is perpendicular to the substrate. Energy minimization is performed by accounting for the energy of the tethers, as well as a few additional terms that represent forces acting on the HPDM body

$$E = E_g + E_{el} + E_B + \sum_{i=1}^{N} E_{teth,i} \tag{2}$$

where E_g accounts for gravity and buoyancy, E_{el} accounts for electrostatic repulsion between the particle and the substrate, and E_B accounts for an externally applied biasing force that is generally set to zero. We found that for HPDMs with spherical bodies, we could calculate E_g, in dimensionless multiples of thermal energy (k_BT), as

$$E_g = (R - P_z)R^3(9.92 \times 10^{-12}\ \text{nm}^{-4}) \tag{3}$$

where R is the HPDM's radius and P_z is the z-height of the center of the HPDM. In addition, when using parameters that best-matched our experimental conditions, E_{el} could be described as

$$E_{el} = R(3.21\text{nm}^{-1})\exp\left(-\frac{P_z - R}{\lambda_D}\right) \tag{4}$$

where λ_D = 1.18 nm. The calculations of E_g and E_{el} are shown in Note S2.

To calculate E_{teth}, each tether is modeled as a nonlinear elastic spring with a force-extension relationship that was calculated using the worm-like chain (WLC) model.[59,60] The details of our WLC calculations are written in Note S3, (accompanied by Figures S7−S11). Briefly, the WLC model has no closed-form solution so we used an approximation developed by Petrosyan[60] to calculate the force-extension

https://doi.org/10.1021/acs.jpcb.2c01897
J. Phys. Chem. B 2022, 126, 7495−7509

Table 1. RoloSim Default Parameters

Parameter	Value	Origin
ρ_{fuel}, RNA fuel surface density	50,000 strand/μm2	measured[17]
ρ_{guide}, DNA guide surface density	91,000 strand/μm2	measured[17]
D_{HPDM}, HPDM diameter	5 μm	manufacturer-specified
t_{max}, simulation duration	30 min	user selected
Δt, simulation timestep	30 ms	user selected
k_{clvg}, RNase H cleavage rate	4.3 s^{-1}	optimized here
$k_{on,0}$, max tether formation rate	0.00913 s^{-1}	optimized here
k_t, tether tensile scale parameter	3.663 k_BT	optimized here
k_c, tether compression stiffness	142 k_BT nm	optimized here
K^*, tether tensile exponent parameter	0.0045 nm^{-2}	optimized here
k_t^*, transition-state scale parameter	0.8769 k_BT	optimized here
K^*, transition-state exponent parameter	0.00356 nm^{-2}	optimized here

curve (Figure S8). We later found that this representation could accurately represent tether mechanics at large extensions but would fail to report resistance to compression at very small extensions. To compensate for this issue, we adapted a Monte Carlo simulation method presented by Becker, Rosa, and Everaers[61] to understand E_{teth} with both extension and compression. Ultimately, we developed a simple, accurate approximation that accurately fits the Monte Carlo simulation data (Figure S9) for E_{teth} as a function of the tether's end-to-end extension, r

$$E_{teth} \approx \kappa_t \exp(Kr^2) + \frac{\kappa_c}{r_z} \tag{5}$$

where κ_t and κ_c are spring constants for extension and compression, respectively, K (in units of nm^{-2}) is a fit parameter that is related to the persistence and contour lengths of the tether, and r_z is the tether's extension in the z-direction. While the first term reflects an energetic cost for extending the tether, the second term reflects an energetic cost for compressing the tether into a small volume between the particle and the substrate. In both cases, the energetic cost is entropic in nature; extension reduces conformational mobility by bringing points on the tether closer to the axis of tension, while compression reduces conformational mobility by confining all points on the tether to a small spaces between the two surfaces.

We performed energy minimization using simulated annealing with six free parameters: three components of a translation vector denoted by $\boldsymbol{D} = [D_x, D_y, D_z]^T$ and three components of a rotation vector denoted by $\boldsymbol{\rho} = [\rho_x, \rho_y, \rho_z]^T$ (using the rotation vector representation, $|\boldsymbol{\rho}|$ denotes the magnitude of the rotation while the orientation of $\boldsymbol{\rho}$ denotes the axis around which the rotation is performed) with an initial guess of $\boldsymbol{D} = \boldsymbol{\rho} = [0,0,0]^T$. Specifically, we used MATLAB (2019b)'s built-in simulannealbnd function (which performs simulated annealing, allowing the system to escape local energetic minimums) with MaxFunctionEvaluations set to 1,000 and an fminunc hybrid function (which performs local gradient descent, allowing the system to find the nearest local energetic minimum following simulated annealing) and otherwise default settings. We performed energy minimization after each timestep in which at least one tether formed, was cleaved or ruptured.

Application of Stochastic Changes. There are three processes that govern the set of tethers bound to the HPDM: association, cleavage, and rupture. Cleavage is mediated by RNase H and occurs with a rate constant of k_{clvg}. Association is described by the rate of duplex hybridization between the RNA fuel and DNA guide strands. This process can be described in an interstrand distance (d)-dependent manner using a Bell model-like equation that relates the energy of the hybridization transition state (E_{tst}) to k_{hyb}

$$k_{hyb} = k_{hyb,0} \exp\left(\frac{-E_{tst}}{k_BT}\right) \tag{6}$$

where $k_{hyb,0}$ is a scaling parameter (i.e., determined during optimization) and E_{tst} is a positive value that is calculated as a function of d by using the WLC model with transition state-specific parameters[62] (Note S3). Ultimately, in a manner similar to what is shown in eq 5, E_{tst} could be accurately approximated using a simple calculation

$$E_{tst} \approx \kappa_t^* \exp(K^* d^2) \tag{7}$$

where κ_t^* and K^* are analogous to κ_t and K but are specific to the transition state tether. To calculate k_{rup}, we use an adaptation[30] of a duplex rupture model presented by Mosayebi et al.[63] that simplifies to

$$k_{rup} = (2.84 \times 10^{-8} s^{-1}) \exp\left(\frac{F}{1.96\ pN}\right) \tag{8}$$

where F vs r is calculated with the WLC model as described above. For computational efficiency, k_{rup} was calculated as a function of r^2 and saved as a lookup table, which was then loaded at the beginning of each RoloSim iteration and referenced (via interpolation) throughout the simulation.

For each timestep, the rate constant for each event (association, rupture, or cleavage) is calculated. If $\exp(-k\Delta t)$ (where k is the rate constant for the event and Δt, generally 30 ms, is the timestep duration) is smaller than a random number on the interval 0 to 1, the event occurs. If any events occur during a timestep, then energy minimization is performed. Energy minimization and the application of stochastic changes are performed iteratively until the simulation reaches 30 min. While the number of possible cleavage and rupture events are both equivalent to the number of tethers ($\sim 10^2$ under standard conditions), the number of possible association events is vastly larger ($\sim 10^7$ under standard conditions). Accordingly, several data management strategies, which make RoloSim computationally tractable by significantly decreasing the number of computations, are used as described in the **user guide**.

Measurement of Simulated HPDM Stall Force and Velocity. To estimate stall force, a 30 min (in simulation

https://doi.org/10.1021/acs.jpcb.2c01897
J. Phys. Chem. B 2022, 126, 7495−7509

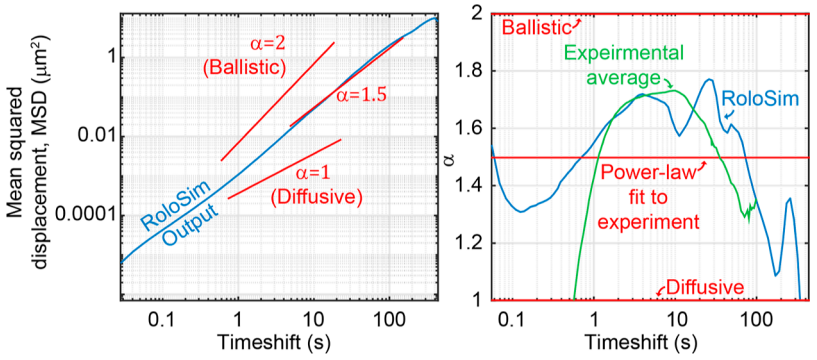

Figure 2. MSD analysis of optimized RoloSim results.

time) simulation of HPDM motion was first run. Next, the simulation's output file was used to re-initialize the simulation at a randomly selected timepoint, excluding the first few minutes and periods of self-entrapment. A random tether was then transformed into an indestructible tether that could neither be cleaved nor ruptured. The simulation was then allowed to run until the total polyvalency dipped below five, and the force experienced by the indestructible tether was measured at each timestep. The tether force was then smoothed over a 1-s window, and the highest force was saved (Figure S13). This process was then repeated 100 times, and the median of the 100 recorded max force values was considered the stall force, F_{HPDM}. When multiple iterations of HPDM translocation were run at a single condition, each of the 100 repetitions was selected randomly from one of the iterations. For each iteration, v_{avg} was calculated by averaging the velocity measured at 20 s intervals (in simulation time) taken from throughout the simulation. When multiple iterations of RoloSim were run at a single condition, v_{avg} was obtained by averaging the v_{avg} values calculated for each iteration.

Optimization of RoloSim. Our process of RoloSim parameter optimization is presented in Note S4, and our optimized parameters are shown in Table 1. To summarize, we varied dynamic parameters (k_{clvg} and $k_{on,0}$) as well as mechanical parameters (κ_c, κ_t, and κ_t^*) to maximize agreement between simulation results and experimental observations of HPDM translocation. Specifically, we sought to reproduce metrics such as the width and depth of the HPDM track, velocity, path persistence, force, and RNase H cleavage rate. We also sought to obtain mechanical parameters that were consistent with the best estimates calculated using well-validated WLC models of force-dependent oligonucleotide hybridization kinetics.

We were unable to accurately reproduce all experimentally relevant observations with any single set of parameters. For example, we could not find a combination of k_{clvg} and $k_{on,0}$ values that simultaneously enabled (1) the use of parameters calculated directly from WLC models, (2) HPDM forces of 100 + pN, and (3) experimentally observed depletion track width and depth (380 nm track width and consumption of 50% of fuel within the depletion track, respectively[17]). As such, we focused on optimizing average velocity (v_{avg}) and stall force (F_{stall}), which are the two main quantities for which we want to understand the scaling laws. Ultimately, we chose to move forward with mechanical parameters κ_c and κ_t that were 10× stiffer than predicted from our WLC models. Our optimized k_{clvg} and $k_{on,0}$ constants are shown in Table 1.

Key Assumptions. The computational tractability of RoloSim rests on two key assumptions centered on the energy minimization approach. First, the HPDM's position and orientation are updated to the energetic minimum during each timestep. In other words, the HPDM's orientation and position during each timestep are essentially represented with a mean-field approximation. This approach neglects two important physical processes that occur in reality: (1) non-instantaneous relaxation dynamics and (2) thermal fluctuations of the HPDM body. We performed simulations to assess the effect of ignoring each of these effects.

First, we assessed the effect of instantaneously updating the HPDM position and orientation at each timestep by calculated the expected dynamics of HPDM relaxation following the formation of a new tether (Note S5). Specifically, we calculated the acceleration, velocity, and displacement at a range of force imbalances, lateral displacements, and HPDM z-heights. For these calculations, we considered the effect of viscous drag due to motion parallel to a nearby surface. For each scenario, we calculated the relaxation time as the duration required for the HPDM to traverse 90% of its total displacement. The relaxation time was substantially shorter than the 30 ms timestep in all conditions, with an average of 2.4 ms (Note S5). We expect that similar findings would hold for rotation and for relaxation following tether cleavage or rupture. Accordingly, these results suggest that instantaneous translation and rotation is a reasonable approximation that reduces the computational cost of RoloSim by orders of magnitude.

Second, we simulated thermal fluctuations of the HPDM position and orientation using the Metropolis-Hastings methods (Note S6). To accomplish this, we restarted completed RoloSim simulations at random timepoints and simulated random translation and reorientation with polyvalencies ranging from 1 to 100 tethers. We calculated the average k_{on} values for pairs of DNA and RNA strands throughout the simulation and compared these thermally averaged k_{on} values to the k_{on} value at the energetic minimum. We found that, at all polyvalencies, the two k_{on} estimates were highly similar as long as the two strands were within a cutoff distance. The energetic-optimum k_{on} for pairs of strands with distances above this cutoff systematically underestimated the thermally averaged k_{on}. However, this cutoff distance increased with increasing polyvalency, such that the fraction of association events above the cutoff decreased with increasing polyvalency. At a polyvalency of 20, fewer than 5% of all association events occurred between strands with interstrand distances above this cutoff distance. This percentage is orders

https://doi.org/10.1021/acs.jpcb.2c01897
J. Phys. Chem. B 2022, 126, 7495−7509

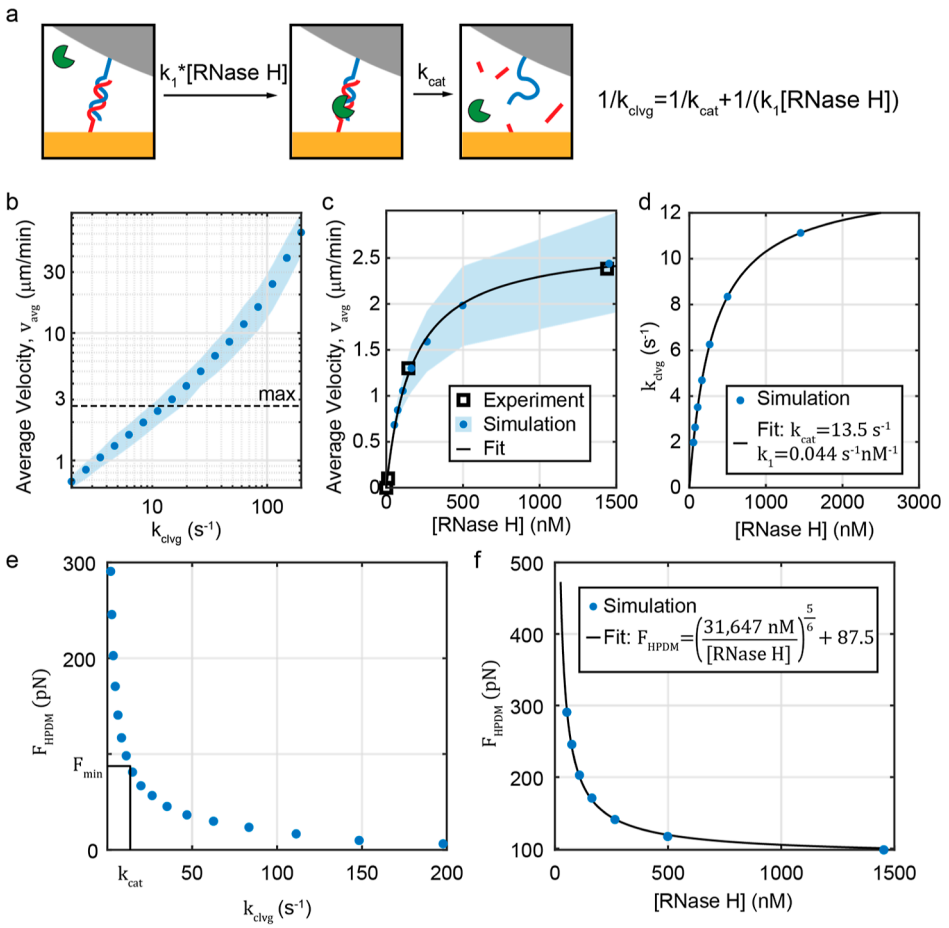

Figure 3. [RNase H]-dependence of F_{HPDM} and v_{avg} (**a**) Sequential reaction scheme used to model RNase H-mediated tether cleavage. The equation demonstrates how k_{clvg} depends on [RNase H], k_1 (the rate constant for the [RNase H]-dependent association step), and k_{cat} (the rate constant of the [RNase H]-independent cleavage step). (**b**) Simulated v_{avg} (median with 25−75% percentiles) vs k_{clvg} on a log−log scale. Dashed line denotes the cutoff velocity corresponding to maximum v_{avg} according to fit to experimental data. (**c**) v_{avg} vs [RNase H] showing both experimental averages[17] (black boxes) and simulation results (median with 25%−75% percentiles) following parameter optimization. Black curve shows a hyperbolic function fit with $v_{avg,max}$ = 2.7 μm/min and $[RNase\ H]_{50}$ = 170 nM. (**d**) k_{clvg} vs [RNase H] following parameter fitting to match the simulation's hyperbolic fit with the experimental hyperbolic fit. Black curve shows fit and blue points show calculations at the k_{clvg} values that were used. (**e**) Simulated F_{HPDM} as a function of k_{clvg}. (**f**) F_{HPDM} as a function of [RNase H]. The power-law fit curve shows an asymptote of F_{min} = 87.5 pN, suggesting that tuning [RNase H] can only be used to decrease F_{HPDM} by a limited amount.

of magnitude lower for typical polyvalencies (100−200 tethers) seen in RoloSim that are typical. As will be discussed near the end of this article, the vast majority (~97%) of RoloSim simulations conducted in this work had higher average polyvalencies than 20 tethers. Accordingly, we conclude that the assumption that the HPDM rests at its energetic minimum during each timestep is a reasonable assumption with minimum effects on HPDM dynamics.

Mean-Squared Displacement Analysis. We started our analysis of the RoloSim outputs by analyzing the condition that we elected to move forward with as our optimal condition (parameters shown in Table 1). Specifically, we analyzed the mean-squared displacement (MSD) properties of the simulated HPDMs' trajectories. We previously found that, when MSD was recorded on a timescale of ~5 s to ~1 min, MSD scaled as a function of $t^{1.5}$. This behavior is a feature of superdiffusive motion, owing in this case to the semi-persistence (i.e., biased toward continuing motion in the current direction of motion) and self-avoiding (i.e., avoidance of crossing depletion tracks) character of HPDM translocation. If the scaling exponent (generally called α) is equal to 1, behavior is diffusive. Generally, α = 2 defines ballistic motion, α < 1 defines subdiffusive motion, and α > 1 defines superdiffusive motion. We found that HPDMs simulated using RoloSim also exhibit superdiffusive motion, with $\alpha \approx 1.5$ when analyzed on experimentally relevant timescales (Figure 2).

A log−log plot of MSD vs. timeshift (τ) exhibits a slope that is equal to the α coefficient when MSD $\propto \tau^{\alpha}$ (left). Running an MSD analysis for the optimized RoloSim output shows that at experimentally relevant timescales (τ ranging from 5 s to ~2 min), α is centered around 1.5, and decays to 1 (diffusive) at longer timescales (right). These findings are consistent with experimental observations.[17,25,26,30] A green curve on the right plot shows the average of ~120 HPDMs tracked at high temporal resolution (~30 Hz) for 5 min.

Use of RoloSim to Parameterize RNase H Kinetics. We next optimized the RNase H cleavage kinetics (Figure 3). We previously observed[17,25] that v_{avg} increases with [RNase H] in a hyperbolic manner; at the standard concentration of [RNase H] = 144 nM, v_{avg} = 1.3 μm/min. Decreasing [RNase H] 10-fold to [RNase H] = 14.4 nM resulted in a near-complete abrogation of motion, while increasing [RNase H] 10-fold to

https://doi.org/10.1021/acs.jpcb.2c01897
J. Phys. Chem. B 2022, 126, 7495−7509

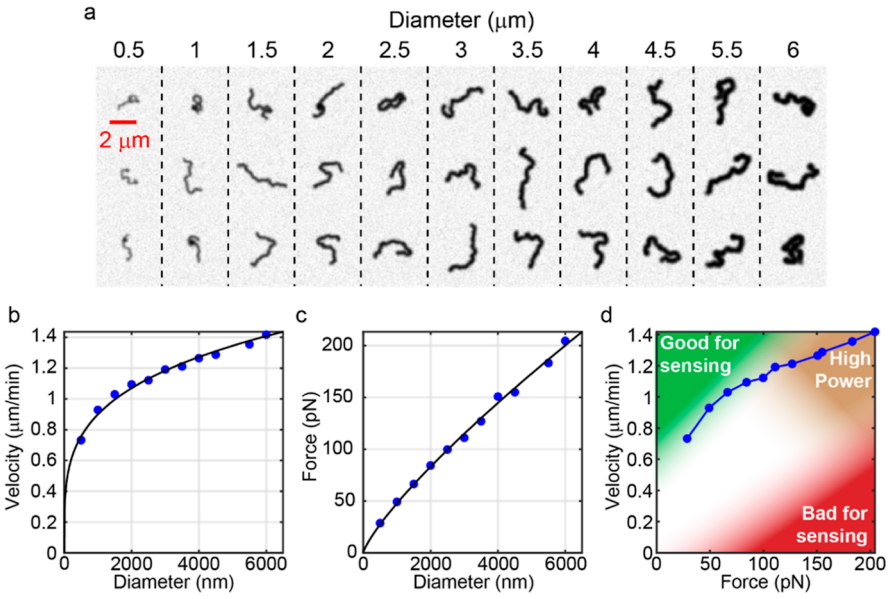

Figure 4. Dependence of F_{HPDM} and v_{avg} on HPDM diameter. (**a**) Montage of depletion tracks obtained with 10 different HPDM diameters ranging from 500−6000 nm. Three 30 min simulations were performed at each diameter. (**b,c**) Plots of average velocity (**b**) and F_{HPDM} (**c**) along with power-law fit curves. (**d**) Plot of velocity vs. force, along with color depiction of regimes on this plot that are good/bad for molecular sensing or that provide a high mechanical power output.

[RNase H] = 1,440 nM resulted in a ∼2-fold increase in v_{avg} to v_{avg} = 2.4 μm/min. We fit the v_{avg} values from Yehl et al.[17] to a hyperbolic function

$$v_{avg} = \frac{v_{avg,max}[\text{RNase H}]}{[\text{RNase H}] + [\text{RNase H}]_{50}} \quad (9)$$

where $v_{avg,max}$ is the maximum HPDM velocity when $k_{clvg} = k_{cat}$ (i.e., when [RNase H] = ∞) and $[\text{RNase H}]_{50}$ is the concentration of RNase H that produces $v_{avg} = v_{avg,max}/2$. We obtained best-fit values of $v_{avg,max}$ = 2.7 μm/min and $[\text{RNase H}]_{50}$ = 170 nM (Figure 3c).

One mechanistic interpretation for this scaling behavior is that RNase H-mediated tether cleavage can be described by a two-step sequential reaction (Figure 3a). The first step, which is [RNase H]-dependent, reflects association of the RNase H molecule with the tether and is described by the pseudo-first-order rate constant k_1. The second step is [RNase H]-independent and reflects cleavage of the RNA backbone of the tether. This step is described by the zero-order rate constant k_{cat}. In this scenario, k_{clvg} can be described in terms of these two rate constants with the standard equation for a sequential two step reaction

$$\frac{1}{k_{clvg}} = \frac{1}{k_1[\text{RNase H}]} + \frac{1}{k_{cat}} \quad (10)$$

Because the second round of optimization produced RoloSim results with varying $k_{on,0}/k_{clvg}$ ratios (see Note S4), we next sought to recycle these optimization results to investigate the effect of tuning k_{clvg} on F_{HPDM}. Perhaps more importantly, we sought to use RoloSim to understand how F_{HPDM} would scale with [RNase H] (which, unlike k_{clvg}, is experimentally tunable in a straightforward manner). To accomplish this, we temporally re-scaled each simulation's output such that $k_{on,0}$ would equal the optimized value of $k_{on,0}$ = 0.0091 and calculated v_{avg} at each condition. We found that 8 of the 17 conditions exhibited $v_{avg} < v_{avg,max}$ (Figure 3b). We then used these eight v_{avg} values and least-squared-residuals fitting to find a combination of k_1 and k_{cat} that resulted in simulated [RNase H] vs v_{avg} values producing best-fit values of $v_{avg,max}$ = 2.7 μm/min and $[RNase\ H]_{50}$ = 170 nM (Figure 3c). The result of this process revealed that k_1 = 0.044 s^{-1} nM^{-1} and k_{cat} = 13.5 s^{-1} (Figure 3d).

This best-fit k_{cat} value is 33-fold higher than the previous k_{cat} value that was measured experimentally[17] of 0.4 s^{-1}. While it is possible that the experimental measurement resulted in an underestimation of k_{cat}, we find it much more likely that the simulation-based estimate is less accurate. We therefore caution against over-interpretation of this finding. Nonetheless, these extracted values can offer some insights into the potential scaling between F_{HPDM} and [RNase H], which could potentially allow F_{HPDM} to be tuned up or down depending on the application.

Relationship between [RNase H] and F_{HPDM}. To understand how [RNase H] could be adjusted to tune F_{HPDM}, we utilized our fit results from the previous subsection. Our results reveal a negative correlation between [RNase H] and F_{HPDM}. Specifically, we found that F_{HPDM} could be fit to a simple power-law relationship

$$F_{HPDM} = \left(\frac{31{,}647\ \text{nM}}{[\text{RNase H}]}\right)^{5/6} \text{pN} + 87.5\ \text{pN} \quad (11)$$

However, according to this model, k_{clvg} can only be tuned as high as k_{cat}, at which point F_{HPDM} converges to 87.5 pN. Therefore, F_{HPDM} can only be reduced—to a point—by increasing [RNase H]. Notably, increasing [RNase H] decreases motor force while also increasing motor speed. Extrapolation of our fit to low [RNase H] does suggest that F_{HPDM} can be tuned to arbitrarily high levels, but this interpretation may be an artifact of our temporal scaling method. Nonetheless, our results suggest that F_{HPDM} can potentially be increased by decreasing [RNase H].

Effect of HPDM Diameter on F_{HPDM} and V_{avg}. To understand how HPDM force and speed scale with HPDM

https://doi.org/10.1021/acs.jpcb.2c01897
J. Phys. Chem. B 2022, 126, 7495−7509

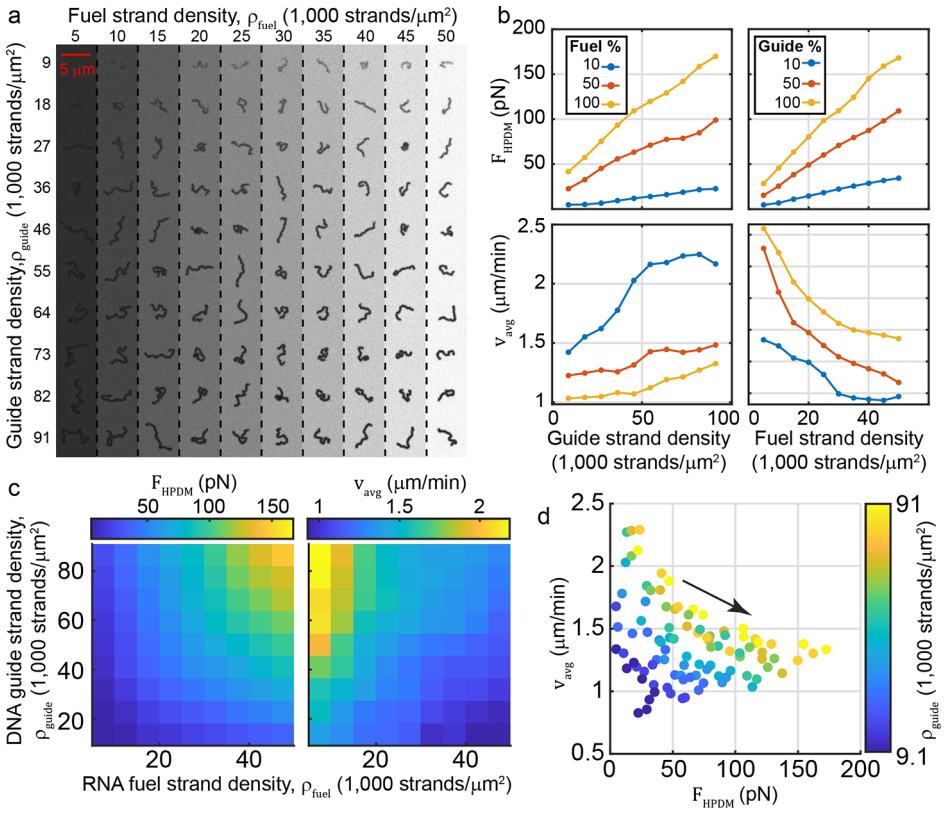

Figure 5. Dependence of F_{HPDM} and v_{avg} on RNA fuel and DNA guide density. (**a**) Montage of simulated depletion tracks obtained with varying DNA guide and RNA fuel strand surface densities. (**b**) F_{HPDM} (top) and v_{avg} (bottom) as a function of guide strand density (left) and fuel strand density (right) at three representative fuel strand and guide strand densities, respectively. (**c**) Surface plots showing F_{HPDM} (left) and v_{avg} (right) as a function of guide and fuel strand density. (**d**) Plot of v_{avg} vs F_{HPDM}, with color depicting guide strand density and a black arrow showing the general direction along which fuel strand density increases.

diameter, D_{HPDM}, we simulated HPDM motion with HPDM diameters ranging in 500 nm increments from 500 to 6,000 nm. Our results (Figure 4) show a near linear dependence of F_{HPDM} (Figure 4c) on D_{HPDM}, fitting accurately ($R^2 > 0.99$) to the relationship

$$F_{HPDM} \approx (0.19\ \text{pN})(D_{HPDM}\ \text{nm}^{-1})^{4/5} \tag{12}$$

In contrast, we found that v_{avg} exhibited highly sub-linear scaling (Figure 4b) with respect to D_{HPDM}, fitting well to the relationship

$$v_{avg} \approx \left(0.16\frac{\mu\text{m}}{\text{min}}\right)(D_{HPDM}\text{nm}^{-1})^{1/4} \tag{13}$$

The nature of this scaling suggests that reduction of HPDM diameter may be one means of improving HPDMs' utility as single-molecule sensors; if HPDM mobility is used as a readout with stalling corresponding to the detection of a target molecule of interest, then it is desirable to have (1) high baseline velocity, which both ensures that the stalling event results in a larger change in the readout metric and also ensures that target molecules are sampled at a higher rate, and (2) low force, which ensures that a smaller number of target molecules (ideally one) can stall an HPDM without being ruptured. These results suggest that decreasing diameter decreases F_{HPDM} to a larger extent than it decreases v_{avg}. Put another way, a 50% reduction in diameter results in a 50% reduction in F_{HPDM} but only decreases v_{avg} by ~10−20%. However, HPDM diameter must remain large enough for HPDMs to be seen using a brightfield microscope, and low polyvalency (which can result from decreased diameter) increases the possibility of spontaneous track detachment. Therefore, future efforts to use smaller HPDMs as more sensitive molecular sensors will likely need to balance these tradeoffs.

We next investigated the effect of RNA fuel and DNA guide strand density on HPDM translocation and force-generation. We ran 100 simulations—one at each combination of ten RNA fuel and DNA foot surface densities (ρ_{fuel} and ρ_{guide}) ranging in 10% increments from 10 to 100% of the experimentally measured density (Figure 5). Our results reveal a near-linear dependence of F_{HPDM} on both ρ_{fuel} and ρ_{guide} and fit well (R^2 = 0.975) to the relationship

$$F_{HPDM} = (10^{-5}\text{pN})\left(\rho_{guide} \times \rho_{fuel}\left(\frac{\mu\text{m}^2}{\text{strands}}\right)^2\right)^{3/4} \tag{14}$$

However, the dependence of v_{avg} on both ρ_{fuel} and ρ_{guide} was not quite as straightforward; v_{avg} was positively correlated with ρ_{guide} and negatively correlated with ρ_{fuel}. Importantly, both correlations were mild; v_{avg} can be approximated with moderate accuracy (R^2 = 0.91) with the function

$$v_{avg} = \left(2\frac{\mu\text{m}}{\text{min}}\right)\left(\frac{\left(\rho_{guide}\frac{\mu\text{m}^2}{\text{strands}}\right)^{1/5}}{\left(\rho_{fuel}\frac{\mu\text{m}^2}{\text{strands}}\right)^{1/4}}\right) \tag{15}$$

These results suggest that decreasing ρ_{fuel} and ρ_{guide} have different overall effects; while decreasing ρ_{guide} decreases both

https://doi.org/10.1021/acs.jpcb.2c01897
J. Phys. Chem. B 2022, 126, 7495−7509

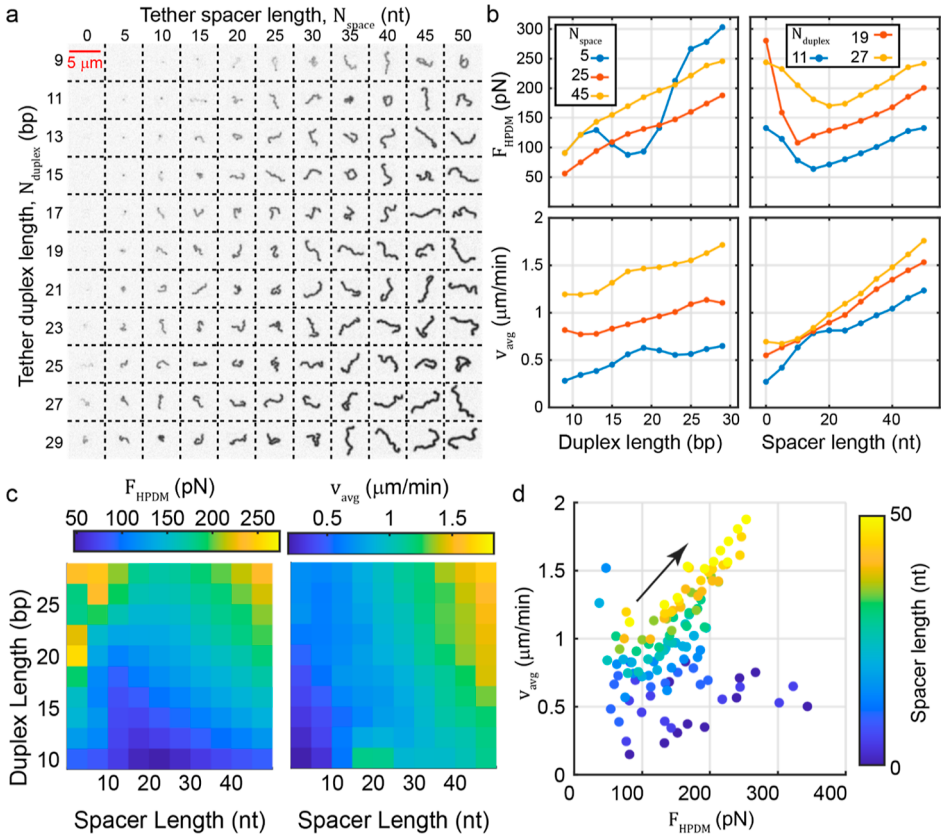

Figure 6. Dependence of F_{HPDM} and v_{avg} on the tether duplex and spacer length. (**a**) Montage of simulated depletion tracks obtained with varying tether spacer and duplex lengths. (**b**) F_{HPDM} (top) and v_{avg} (bottom) as a function of duplex length (left) and spacer length (right) at three representative spacer and duplex lengths, respectively. (**c**) Surface plots showing F_{HPDM} (left) and v_{avg} (right) as a function of tether duplex and spacer length. (**d**) Plot of v_{avg} vs F_{HPDM}, with color depicting spacer length and a black arrow showing the general direction along which duplex length increases.

F_{HPDM} and v_{avg}, decreasing ρ_{fuel} decreases F_{HPDM} and increases v_{avg}. In the latter case, both effects drive the HPDM toward a parameter space that we identified in the previous section as favorable for molecular sensing purposes (high speed and low force). In fact, decreasing ρ_{fuel} from 50,000 strands/μm^2 10-fold to 5,000 strands/μm^2 while preserving ρ_{guide} at 91,000 strands/μm^2 reduces F_{HPDM} to ~23 pN—which is sufficient for single molecule detection of high-affinity bonds such as DNA duplexes or high-affinity antibody−antigen interactions—and almost doubles v_{avg} from 1.3 to 2.5 μm.

As mentioned at the close of the previous section, any change that reduces the average polyvalency of the HPDM may also result in an increase in the rate of spontaneous HPDM detachment−which is unfavorable. Furthermore, RoloSim does not model nonspecific interactions between the HPDM and the substrate, but the persistent presence of immobile particles in HPDM tracking experiments suggests that some fraction of HPDMs stick to the surface via nonspecific interactions. It is possible that reducing ρ_{fuel} may alter the nature of these interactions. Furthermore, it is possible, as with all modeling results presented here, that our predictions may not be consistent with future experiments due to the nuances of surfaces and interfaces that are not captured by our simulation. This is particularly important to keep in mind when considering the ρ_{fuel}-dependent results because the experimentally measured track depth is ~50%, while here it is ~100%. Nonetheless, our results suggest that reducing ρ_{fuel} while maintaining high ρ_{guide} may be an effective strategy for using HPDMs as molecular sensors.

Effect of Tether Duplex and Spacer Length on F_{HPDM} and V_{avg}. We next examined the effect of tether spacer and duplex length on HPDM translocation (Figure 6). Specifically, we tested all combinations of 11 duplex lengths (N_{duplex}, ranging from 9 to 29 bp) and 11 spacer lengths (N_{spacer} ranging from 0 to 50 nt). For each combination, we performed WLC Monte Carlo simulations as described in Note S3 and fit κ_t, κ_c, and **K** parameters of the calculated energy−extension curve to eq 5. We also performed this process for the hybridization transition state. We then scaled the κ_t and κ_c parameters 10×, in accordance with our optimization results.

As in the above analysis of surface density, force increased both with spacer length and duplex length. Mobility was very poor (with HPDMs largely being detached from the track) at low spacer and duplex lengths, rendering force and velocity estimates volatile and largely meaningless. However, at spacer lengths greater than 15 nt, F_{HPDM} fit well (R = 0.96) to the relationship

$$F_{HPDM} = (2.5\ \text{pN})\left(\frac{N_{spacer}}{\text{nt}}\right)^{1/2}\left(\frac{N_{duplex}}{\text{bp}}\right)^{4/5} \quad (16)$$

and v_{avg} also scaled meaningfully with both N_{spacer} and N_{duplex}, fitting well to the relationship

https://doi.org/10.1021/acs.jpcb.2c01897
J. Phys. Chem. B 2022, 126, 7495−7509

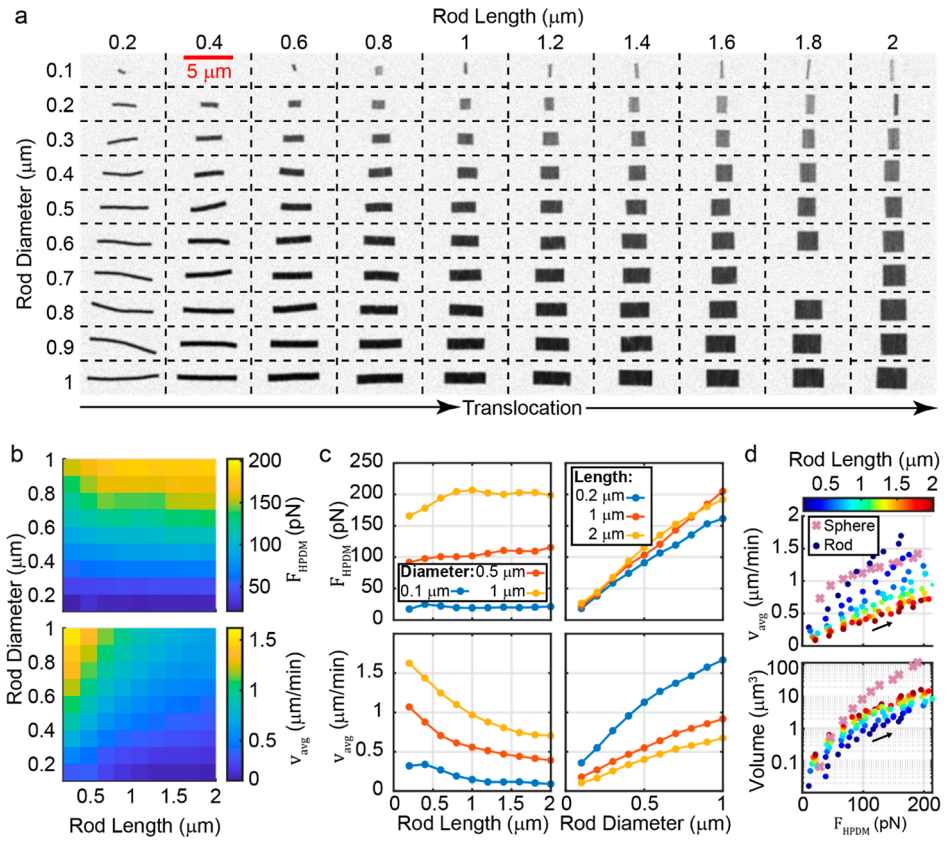

Figure 7. Results of simulations of rod-shaped HPDMs (rHPDMs). (**a**) Montage of simulated depletion tracks obtained with varying rHPDM lengths and diameters. The direction of translocation is generally right to left or left to right (not up/down). (**b**) Surface plots showing F_{HPDM} and v_{avg} as a function of rod length and rod diameter. (**c**) F_{HPDM} and v_{avg} as a function of rod length (left) and rod diameter (right) at three representative rod diameters and rod lengths, respectively. (**d**) Scatterplots of v_{avg} and HPDM volume vs F_{HPDM} with color depicting rod length and black arrows showing the general direction along which rod diameter increases. The results of spherical HPDMs with varying diameter are shown as x's. Note the large differences between the volume (plotted on a log-scale) of spheres and rods at similar force levels.

$$v_{avg} = \left(0.055\frac{\mu m}{min}\right)\left(\frac{N_{spacer}}{nt}\right)^{3/5}\left(\frac{N_{duplex}}{bp}\right)^{1/3} \quad (17)$$

It is important to note that these results were obtained with different strand lengths but the same strand surface densities. However, it is likely that strand length influences surface density due to crowding effects. In addition, from a practical standpoint changing the duplex length should also affect the effective k_{clvg} because a longer duplex will require more individual cleavage events in order to yield complete tether detachment. However, as these simulations were all performed using the same k_{clvg} values, simply tuning the duplex length experimentally may not produce the same effects observed in this study.

Simulations of Rod-Shaped HPDMS. Our studies of HPDMs thus far have focused on spherical HPDMs, but rod-shaped HPDMs (rHPDMs) offer a means of substantially reducing HPDM size. To understand the characteristics (v_{avg} and F_{HPDM} in particular) of rHPDMs, we used RoloSim to simulate rods (specifically, cylinders with spherical tips) with diameters (D_{rod}) ranging from 100 to 1,000 nm and lengths L_{rod}) ranging from 200 to 2000 nm (Figure 7). Interestingly, our results suggest that rod diameter is much more important than rod length in determining both v_{avg} and F_{HPDM}; while increasing diameter increased both F_{HPDM} and v_{avg} in a near linear manner, increasing rod length decreased v_{avg} and had a very mild effect on F_{HPDM}. We found that F_{HPDM} could be accurately described (R^2 = 0.986) by the equation

$$F_{HPDM} = (0.5\ pN)((D_{rod}\ nm^{-1})^{4/5}(L_{rod}\ nm^{-1})^{1/14}) - 11.4\ pN \quad (18)$$

which illustrates minimal dependence of F_{HPDM} on L_{rod} but strong dependence on D_{rod}. We found v_{avg} could be accurately described (R^2 = 0.957) by the equation

$$v_{avg} = \left(0.1466\frac{\mu m}{min}\right)\left(\frac{(D_{rod}\ nm^{-1})^{3/5}}{(L_{rod}\ nm^{-1})^{1/3}}\right) \quad (19)$$

Importantly, rHPDMs offer a means of taking the force-generating properties of autochemophoresis to a much smaller length scale than is currently possible. For example, the rHPDM with D_{rod} = 700 *nm* and L_{rod} = 600 *nm* generates a similar level of force (F_{HPDM} = 150 pN) to 5 μm spherical HPDMs but is ∼160× smaller by volume (or 280× if the spherical caps—which largely do not contribute to rHPDM motion—are removed).

These initial findings suggest major challenges in creating nanoscale (i.e., <100 nm in their smallest dimension) autochemophoretic motors that can generate force in the high pN range. Because rods with D_{rod} = 100 nm never generate more than ∼20 pN of force, long thin rods do not appear to be capable of producing arbitrarily high forces. In

https://doi.org/10.1021/acs.jpcb.2c01897
J. Phys. Chem. B 2022, 126, 7495−7509

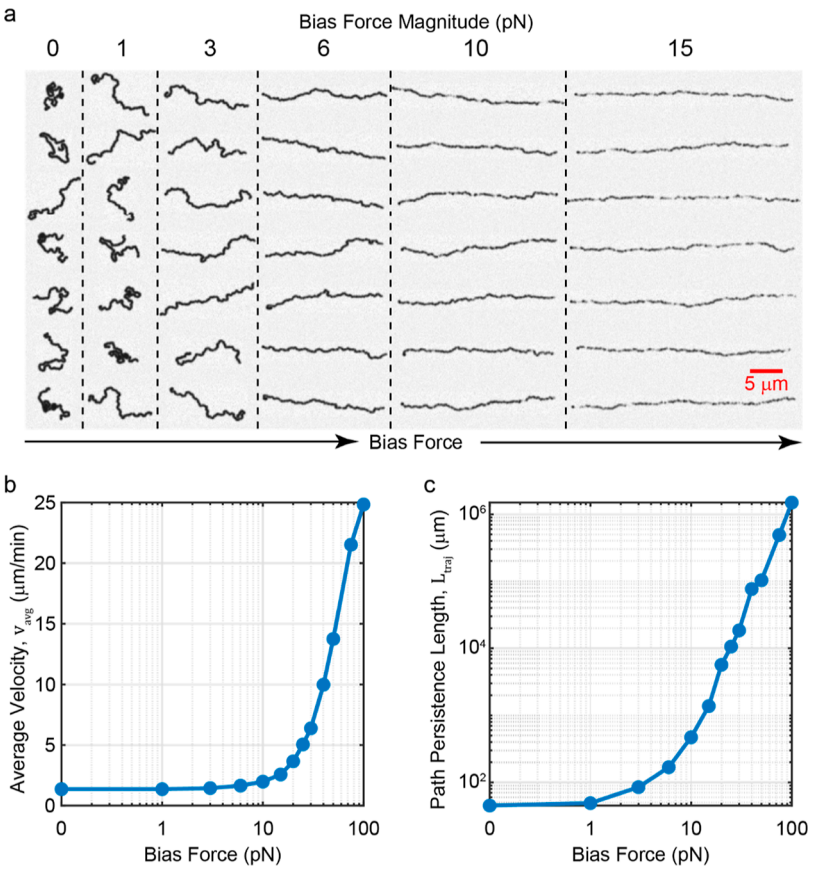

Figure 8. Simulation results of HPDM translocation in the presence of a biasing force. (**a**) Montage of simulated depletion track images from simulations of HPDMs rolling in the presence of biasing forces (pointing to the right) at varying force magnitudes. (**b,c**) Quantification of v_{avg} and L_{traj} as a function of the bias force magnitude.

theory, short wide "rods" (e.g., L_{rod} = 100 nm, D_{rod} = 1000 nm) may be capable of generating high forces, but such "cheese-wheel"-type rods would have very large volumes because they would be micron-scale in two dimensions, which essentially defeats the purpose of size reduction. In theory, F_{HPDM} could be increased for thin rods by decreasing [RNase H] (Figure 3), at the cost of v_{avg}. Finally, it is important to note that this discussion would likely be slightly different if rHPDMs had been simulated without spherical caps, which mildly influence the track width.

HPDM Motion with a Biasing Force. To complete this initial adhesive dynamics study of HPDM translocation, we investigated the effect of a biasing force on HPDM translocation. Because HPDMs "write" as they translocate by removing RNA fuel (or by depositing molecules through mechanical bond rupture[30]), the ability to control HPDM direction would enable a new form of highly parallel nanolithography. However, it is unclear whether HPDM directionality can be controlled using an external biasing force. To address this question, we used RoloSim to evaluate the effect of an externally applied biasing force on HPDM motion. We ran seven iterations at each of 11 biasing force magnitudes, ranging from 0 to 100 pN. At each condition, we quantified the path persistence length (L_{traj}) and v_{avg} to assess the extent to which the biasing force directs and speeds up HPDM translocation.

Our results (Figure 8) suggest that HPDM motion can be directed using a biasing force. A force of 1 pN results in no discernible change in directionality, L_{traj}, or v_{avg}. However, a force of 3 pN creates a clear bias in HPDM motion toward the direction of the force. This bias magnitude does not result in a notable increase in v_{avg}, and tracks still exhibit many notable deviations from the most favorable direction of translocation, but there is a notable increase in L_{traj}. A biasing force of 6 pN further increases L_{traj} and further increases the directional appearance of the depletion track. A biasing force of 10 pN results in a notable increase in L_{traj} and v_{avg} and also appears to result in periodic detachment from the depletion track. Forces above 10 pN result in exponentially increasing L_{traj} values, linearly increasing v_{avg} values, and an increased frequency of apparent detachment events.

The apparent detachment events appear to be an artifact of the manner in which RoloSim handles detachment; when the polyvalency reduces to zero, the HPDM undergoes planar Brownian motion until a new tether forms. In other words, the HPDM is not allowed to detach and irreversibly flow away from the surface following detachment of the final tether, as would be expected to happen in reality. Accordingly, our RoloSim results suggest that as little as 10 pN can result in complete detachment of HPDMs from the surface. Nonetheless, our results suggest that there may be a biasing force range that can steer HPDMs without causing them to detach from the surface.

To assess the accuracy of this final prediction experimentally, we imaged HPDMs rolling under standard conditions ([RNase H] = 144 nM, 100% RNA fuel and DNA guide, 5 μm diameter sphereical HPDMs) while applying a biasing force using flow

https://doi.org/10.1021/acs.jpcb.2c01897
J. Phys. Chem. B 2022, 126, 7495−7509

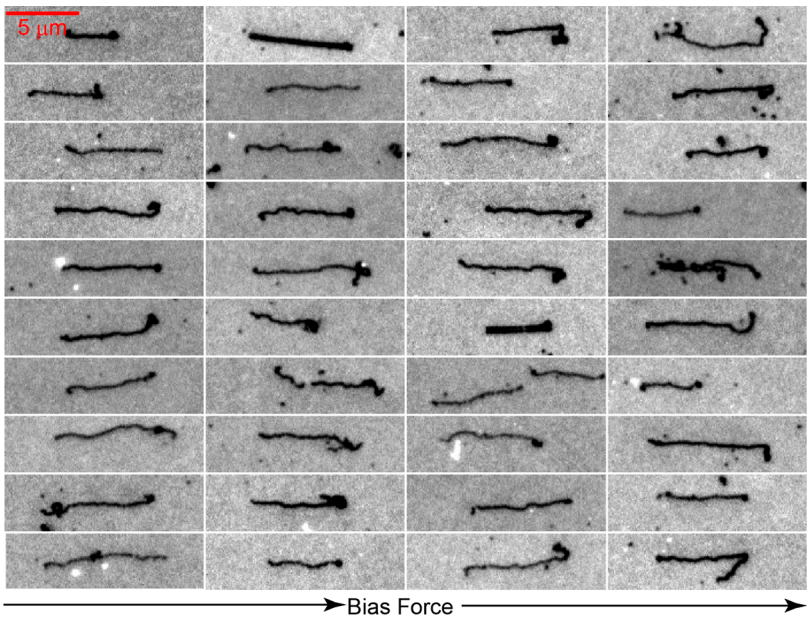

Figure 9. Experimental images of depletion tracks following HPDM translocation with flow-based bias force. This figure shows 40 depletion tracks imaged after ten minutes of HPDM translocation in the presence of flow, followed by 10 minutes of HPDM translocation in the absence of flow. The direction of flow was from left to right, and it was performed at a flow rate of 1000 μL/min. According to our calculations above, this flow rate corresponds to a force of F_{bias} = 19 pN. The depletion tracks generally reveal ∼5−10 μm of translocation from left to right, followed by random self-avoiding translocation.

(Figure 9). We applied flow rates (Q) ranging from 200 μL/min to 1000 μL/min and imaged HPDMs for 10 min.

At a condition of Q = 1000 μL/min, we found that HPDM motion was biased toward the direction of flow in a parallel fashion. To illustrate this, we imaged depletion tracks after 10 min of flow, followed by 10 min of rolling in the absence of flow. We used ibidi μ-Slide VI 0.4 flow cells for this study, which has rectangular channels 3.8 mm in width and 0.4 mm in height. This cross-sectional area and flow rate results in an average flow velocity of ∼11 mm/s. Assuming parabolic flow, (which is reasonable given the channel's small aspect ratio[64]), the velocity at a height of 2.5 μm is

$$v_{flow} = \left(.011\frac{m}{s}\right)\left(1 - \left(\frac{200\ \mu m - 2.5\ \mu m}{200\ \mu m}\right)^2\right) = .00041\frac{m}{s} \quad (20)$$

which, using Stokes law

$$F_{bias} = 6\pi(.0000025\ m)\left(1\frac{Ns}{m^2}\right)\left(.00041\frac{m}{s}\right) = 19\ pN \quad (21)$$

yields F_{bias} = 19 pN. The finding that HPDMs can translocate processively under a 19 pN biasing force is somewhat out of agreement with the RoloSim prediction, which predicted maximum bias at ∼6 pN and detachment at 10 pN. Nonetheless, the experimental and computational results are in good qualitative agreement.

DISCUSSION AND CONCLUSIONS

We have developed a computational method, called RoloSim, for explicitly simulating relatively large-scale burnt bridge ratchet motors. Our simulation approach, which relies on the adhesive dynamics method, resembles previous works but has some key differences. Unlike with other AD simulations of BBR motors, Brownian fluctuations of the microparticle body are ignored and assumed to be effectively suppressed by the large number of tethers constraining the particle's motion.[41,42,49] This limitation may interfere with efforts to accurately simulate BBR motion of smaller motors, for which Brownian fluctuations must be considered. Instead, thermal fluctuations are considered at the level of the individual tethers, which form and dissociate in a kinetic Monte Carlo fashion. Unlike with previous AD simulations of microscale cargos (namely, cells),[65] the driving force for motor translocation is generated internally due to the auto-degradatory activity of individual tethers, rather than externally applied fields.

Using RoloSim, we have uncovered the scaling properties of force-generation and speed as a function of various experimentally tunable parameters such as strand density, tether cleavage rate, HPDM size, and tether length (Figures 10 and 11). Future experimental works will aim to test these predictions. We have also studied the speed and force generation capacity of rod-shaped motors, with our results suggesting that force scales with rod diameter but not with rod length, while speed scales with diameter and decreases with length. These findings suggests that efforts to design BBR nanomotors with high force generating capacity *de novo* will require more sophisticated designs. Future works will utilize RoloSim to explore design options that could enable the development of high-power nanomotors. Our findings also suggest some strategies for tuning motor force and speed. For example, force can be minimized while speed is maximized by creating a large ratio of guide strand surface density to fuel strand surface density.

As an initial test of the validity of our predicted scaling properties, we here compare our predictions with published experimental results. Recent work[25] found that small, 50 nm DNA motors exhibited average velocities of ∼0.18 μm/min. This measurement was performed at lower [RNase H] (30

https://doi.org/10.1021/acs.jpcb.2c01897
J. Phys. Chem. B 2022, 126, 7495−7509

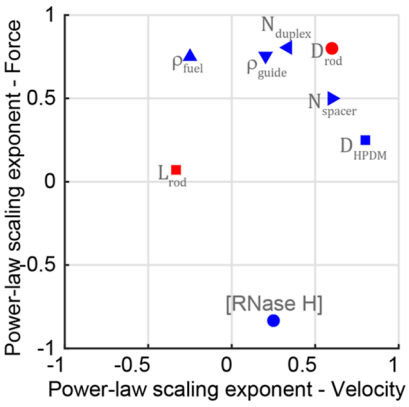

Figure 10. Power law scaling exponent fit parameters for variables studied in this work. This figure shows eight scattered points (each labeled) showing the best-fit power law exponents for force vs. for velocity from fit equations presented throughout this manuscript. Broadly speaking, the power law scaling exponent determines how strongly a variable controls F_{HPDM} or v_{avg}. Variables represented close to the corners of this plot can be used to simultaneously tune both v_{avg} and F_{HPDM}, while variables close to the major axes can be used to tune either F_{HPDM} or v_{avg} without strongly influencing the other.

nM), higher ρ_{guide} (190,000 μm^{-2}), and lower ρ_{fuel} (22,000 μm^{-2}) than the work by Yehl et al. that we used for our initial parameterization[17] (which had 5 μm diameter, [RNase H] = 144 nM, ρ_{guide} = 91,000 μm^{-2}, and ρ_{fuel} = 50,000 μm^{-2}, and yielded v_{avg} = 1.3 μm/min). We applied the scaling relationships fit in this work to account for all these differences

$$\left(\frac{50\text{ nm}}{50{,}000\text{ nm}}\right)^{1/4}\left(\frac{190{,}000\ \mu m^{-2}}{91{,}000\ \mu m^{-2}}\right)^{1/5}\left(\frac{22{,}000\ \mu m^{-2}}{50{,}000\ \mu m^{-2}}\right)^{-\frac{1}{4}}\left(\frac{\left(\frac{30\text{ nM}}{170\text{ nM}+30\text{ nM}}\right)}{\left(\frac{144\text{ nM}}{170\text{ nM}+144\text{ nM}}\right)}\right) = 0.19\frac{\mu m}{\text{min}} \quad (22)$$

yielding a prediction of v_{avg} = 0.19 μm/min, which is remarkably similar to the experimental measurement. Applying a similar analysis to force predicts F_{HPDM} = 1.6 pN. Note that direct simulation of such small DNA motors would likely require explicit consideration of Brownian fluctuations.[66]

A key limitation of RoloSim lies in a parameter assumption that was made in order to enable studies of force scaling; tether stiffness was assumed to be 10 times stiffer than would be predicted from the WLC theory. In addition, RoloSim produces motor depletion tracks that are completely devoid of uncleaved fuel, while experimental findings suggest that ~50% of fuel remains uncleaved. The reason for partial cleavage of the RNA fuel is unclear to us, as the RNA is completely cleaved if soluble complementary DNA and RNase H are added to the solution. Notably, gold nanoparticle motors,[25] DNA origami motors,[26] and other rod-shaped motors[17] all generate tracks with partially cleaved RNA fuel in their wake and thus this experimental observation is robust. Super-resolution imaging, FRET or perhaps fluorescence correlation-based analysis of the RNA conformation at the junction is needed to shed more light on this question. That said, nanoscale interfaces, such as the motor-surface junction, are notoriously difficult to characterize experimentally

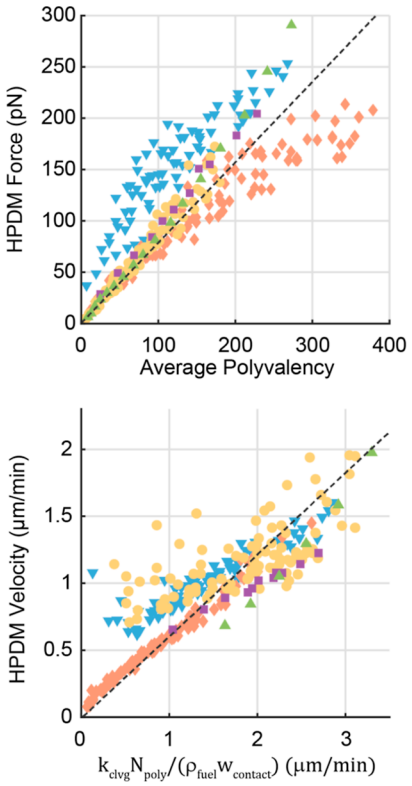

Figure 11. Summary of scaling predictions in our studies. These plots show our best efforts to explain force and velocity scaling relationships that are consistent across all scaling studies presented here (Figures 3−7). Each scatter point denotes a single condition, while the color and shape reflect the scaling study. A dashed line shows a linear fit to all scatter points. Green up-pointing triangles: tether cleavage rate (Figure 3). Purple squares: HPDM diameter (Figure 4). Yellow circles: strand density (Figure 5). Blue down-pointing triangles: tether length (Figure 6). Orange diamonds: rHPDMs (Figure 7). The top plot shows an approximate linear scaling (correlation coefficient: 0.82) between F_{HPDM} and the median polyvalency (N_{poly}), which is consistent with previous predictions.[39,55] The bottom plot shows linear scaling (correlation coefficient: 0.88) between v_{avg} and $k_{clvg}N_{poly}/(\rho_{fuel}w_{contact})$, where $w_{contact}$ is the width of the HPDM contact zone (see Note S7 for calculation). This variable can be explained as follows: $k_{clvg}N_{poly}$ is the effective fuel strand consumption rate. Dividing by ρ_{fuel} transforms strand consumption rate into an effective surface area consumption rate. Finally, dividing by $w_{contact}$ transforms area consumption rate into an effective velocity. While this explanatory variable is somewhat definitional and requires a more complicated calculation than the explanatory variable for F_{HPDM}, we nonetheless include it here because it bridges the results from all of our scaling studies.

(especially given the far-from-equilibrium nature of the system), and hence spectroscopic analysis will not be trivial. Future works will be aimed at adjusting the model in order to simultaneously reproduce all experimentally relevant parameters and achieve a more reliable model that recapitulates these aspects of the motor system.

■ ASSOCIATED CONTENT

Supporting Information

The Supporting Information is available free of charge at https://pubs.acs.org/doi/10.1021/acs.jpcb.2c01897.

https://doi.org/10.1021/acs.jpcb.2c01897
J. Phys. Chem. B 2022, 126, 7495−7509

User Guide for RoloSim v1.20 and supplemental notes 1−7, with supplemental figures 1−17 and supplemental table 1 (PDF)

AUTHOR INFORMATION

Corresponding Authors

Aaron T. Blanchard − *Department of Biomedical Engineering, Georgia Institute of Technology and Emory University, Atlanta, Georgia 30322, United States;* Present Address: Current address: Department of Biomedical Engineering, Duke University, Durham, North Carolina, 27709, United States; orcid.org/0000-0002-3129-6591; Email: ATBlanchard@ymail.com

Khalid Salaita − *Department of Biomedical Engineering, Georgia Institute of Technology and Emory University, Atlanta, Georgia 30322, United States; Department of Chemistry, Emory University, Atlanta, Georgia 30322, United States;* orcid.org/0000-0003-4138-3477; Email: k.salaita@emory.edu

Authors

Selma Piranej − *Department of Chemistry, Emory University, Atlanta, Georgia 30322, United States*

Victor Pan − *Department of Biomedical Engineering, Georgia Institute of Technology and Emory University, Atlanta, Georgia 30322, United States;* Present Address: Current address: Intellia Therapeutics, Cambridge, Massachusetts 02139, United States.

Complete contact information is available at: https://pubs.acs.org/10.1021/acs.jpcb.2c01897

Author Contributions

A.T.B. and K.S. conceived of project. A.T.B. developed software and performed experiments, modeling, and simulations and wrote manuscript. V.P. and S.P. assisted with experiments. All authors have given approval to the final version of the manuscript.

Notes

The authors declare no competing financial interest.

ACKNOWLEDGMENTS

This work was supported by the National Science Foundation (NSF) , CHE 2004126 (K.S.), DMR 1905947 (K.S.), NIH 1U01AA029345 (K.S.), and NSF GRFP DGE-1444932 (A.T.B). We thank Professors Eric Weeks and Yonggang Ke (Emory University, GA, USA), Keir Neuman (National Institutes of Health, MD, USA), and Todd Sulcheck (Georgia Institute of Technology, GA, USA) for helpful conversations. This research was supported in part through research cyberinfrastructure resources and services provided by the Partnership for an Advanced Computing Environment (PACE) at the Georgia Institute of Technology, Atlanta, Georgia, USA.[67] This research was conducted at Emory University and the Georgia Institute of Technology. We honor these institutions' land acknowledgments: https://www.emory.edu/home/explore/history/land-acknowledgment/index.html (Emory University) and https://serve-learn-sustain.gatech.edu/serve-learn-sustain-land-acknowledgment (the Georgia Institute of Technology).

REFERENCES

(1) Leidel, C.; Longoria, R. A.; Gutierrez, F. M.; Shubeita, G. T. Measuring molecular motor forces in vivo: implications for tug-of-war models of bidirectional transport. *Biophys. J.* **2012**, *103*, 492−500.

(2) Schliwa, M.; Woehlke, G. Molecular motors. *Nature* **2003**, *422*, 759.

(3) Linke, H.; Höcker, B.; Furuta, K. y.; Forde, N. R.; Curmi, P. M. G. Synthetic biology approaches to dissecting linear motor protein function: towards the design and synthesis of artificial autonomous protein walkers. *Biophys. Rev.* **2020**, *12*, 1041−1054.

(4) Sherman, W. B.; Seeman, N. C. A Precisely Controlled DNA Biped Walking Device. *Nano Lett.* **2004**, *4*, 1203−1207.

(5) Yin, P.; Yan, H.; Daniell, X. G.; Turberfield, A. J.; Reif, J. H. A Unidirectional DNA Walker That Moves Autonomously along a Track. *Angew. Chem., Int. Ed.* **2004**, *43*, 4906−4911.

(6) Shin, J.-S.; Pierce, N. A. A Synthetic DNA Walker for Molecular Transport. *J. Am. Chem. Soc.* **2004**, *126*, 10834−10835.

(7) Bath, J.; Green, S. J.; Turberfield, A. J. A Free-Running DNA Motor Powered by a Nicking Enzyme. *Angew. Chem., Int. Ed.* **2005**, *44*, 4358−4361.

(8) Omabegho, T.; Sha, R.; Seeman, N. C. A Bipedal DNA Brownian Motor with Coordinated Legs. *Science* **2009**, *324*, 67.

(9) He, Y.; Liu, D. R. Autonomous multistep organic synthesis in a single isothermal solution mediated by a DNA walker. *Nat. Nanotechnol.* **2010**, *5*, 778.

(10) Gu, H.; Chao, J.; Xiao, S.-J.; Seeman, N. C. A proximity-based programmable DNA nanoscale assembly line. *Nature* **2010**, *465*, 202.

(11) Lund, K.; Manzo, A. J.; Dabby, N.; Michelotti, N.; Johnson-Buck, A.; Nangreave, J.; Taylor, S.; Pei, R.; Stojanovic, M. N.; Walter, N. G.; Winfree, E.; Yan, H. Molecular robots guided by prescriptive landscapes. *Nature* **2010**, *465*, 206.

(12) Wang, Z.-G.; Elbaz, J.; Willner, I. DNA Machines: Bipedal Walker and Stepper. *Nano Lett.* **2011**, *11*, 304−309.

(13) Wickham, S. F. J.; Bath, J.; Katsuda, Y.; Endo, M.; Hidaka, K.; Sugiyama, H.; Turberfield, A. J. A DNA-based molecular motor that can navigate a network of tracks. *Nat. Nanotechnol.* **2012**, *7*, 169.

(14) You, M.; Chen, Y.; Zhang, X.; Liu, H.; Wang, R.; Wang, K.; Williams, K. R.; Tan, W. An Autonomous and Controllable Light-Driven DNA Walking Device. *Angew. Chem., Int. Ed.* **2012**, *51*, 2457−2460.

(15) Cha, T.-G.; Pan, J.; Chen, H.; Salgado, J.; Li, X.; Mao, C.; Choi, J. H. A synthetic DNA motor that transports nanoparticles along carbon nanotubes. *Nat. Nanotechnol.* **2013**, *9*, 39.

(16) Zhou, C.; Duan, X.; Liu, N. A plasmonic nanorod that walks on DNA origami. *Nat. Commun.* **2015**, *6*, 8102.

(17) Yehl, K.; Mugler, A.; Vivek, S.; Liu, Y.; Zhang, Y.; Fan, M.; Weeks, E. R.; Salaita, K. High-speed DNA-based rolling motors powered by RNase H. *Nat. Nanotechnol.* **2015**, *11*, 184.

(18) Jung, C.; Allen, P. B.; Ellington, A. D. A stochastic DNA walker that traverses a microparticle surface. *Nat. Nanotechnol.* **2015**, *11*, 157.

(19) Wang, L.; Deng, R.; Li, J. Target-fueled DNA walker for highly selective miRNA detection. *Chem. Sci.* **2015**, *6*, 6777−6782.

(20) Dannenberg, F.; Kwiatkowska, M.; Thachuk, C.; Turberfield, A. J. DNA walker circuits: computational potential, design, and verification. *Nat. Comput.* **2015**, *14*, 195−211.

(21) Yang, X.; Tang, Y.; Mason, S. D.; Chen, J.; Li, F. Enzyme-Powered Three-Dimensional DNA Nanomachine for DNA Walking, Payload Release, and Biosensing. *ACS Nano* **2016**, *10*, 2324−2330.

(22) Thubagere, A. J.; Li, W.; Johnson, R. F.; Chen, Z.; Doroudi, S.; Lee, Y. L.; Izatt, G.; Wittman, S.; Srinivas, N.; Woods, D.; Winfree, E.; Qian, L. A cargo-sorting DNA robot. *Science* **2017**, *357*, 6356.

(23) Qu, X.; Zhu, D.; Yao, G.; Su, S.; Chao, J.; Liu, H.; Zuo, X.; Wang, L.; Shi, J.; Wang, L.; Huang, W.; Pei, H.; Fan, C. An Exonuclease III-Powered, On-Particle Stochastic DNA Walker. *Angew. Chem., Int. Ed.* **2017**, *56*, 1855−1858.

(24) Urban, M. J.; Both, S.; Zhou, C.; Kuzyk, A.; Lindfors, K.; Weiss, T.; Liu, N. Gold nanocrystal-mediated sliding of doublet DNA origami filaments. *Nat. Commun.* **2018**, *9*, 1454.

(25) Bazrafshan, A.; Kyriazi, M.-E.; Holt, B. A.; Deng, W.; Piranej, S.; Su, H.; Hu, Y.; El-Sagheer, A. H.; Brown, T.; Kwong, G. A.; Kanaras, A. G.; Salaita, K. DNA Gold Nanoparticle Motors Demonstrate Processive Motion with Bursts of Speed Up to 50 nm Per Second. *ACS Nano* **2021**, *15*, 8427−8438.
(26) Bazrafshan, A.; Meyer, T. A.; Su, H.; Brockman, J. M.; Blanchard, A. T.; Piranej, S.; Duan, Y.; Ke, Y.; Salaita, K. Tunable DNA Origami Motors Translocate Ballistically Over μm Distances at nm/s Speeds. *Angew. Chem., Int. Ed.* **2020**, *59*, 9514−9521.
(27) Wickham, S. F. J.; Endo, M.; Katsuda, Y.; Hidaka, K.; Bath, J.; Sugiyama, H.; Turberfield, A. J. Direct observation of stepwise movement of a synthetic molecular transporter. *Nat. Nanotechnol.* **2011**, *6*, 166−169.
(28) Pei, R.; Taylor, S. K.; Stefanovic, D.; Rudchenko, S.; Mitchell, T. E.; Stojanovic, M. N. Behavior of Polycatalytic Assemblies in a Substrate-Displaying Matrix. *J. Am. Chem. Soc.* **2006**, *128*, 12693−12699.
(29) Šulc, P.; Ouldridge, T. E.; Romano, F.; Doye, J. P. K.; Louis, A. A. Simulating a burnt-bridges DNA motor with a coarse-grained DNA model. *Nat. Comput.* **2014**, *13*, 535−547.
(30) Blanchard, A. T.; Bazrafshan, A. S.; Yi, J.; Eisman, J. T.; Yehl, K. M.; Bian, T.; Mugler, A.; Salaita, K. Highly polyvalent DNA motors generate 100+ piconewtons of force via autochemophoresis. *Nano Lett.* **2019**, *19*, 6977−6986.
(31) Sugawara, T.; Kaneko, K. Chemophoresis as a driving force for intracellular organization: Theory and application to plasmid partitioning. *Biophysics* **2011**, *7*, 77−88.
(32) Wang, W.; Duan, W.; Ahmed, S.; Mallouk, T. E.; Sen, A. Small power: Autonomous nano- and micromotors propelled by self-generated gradients. *Nano Today* **2013**, *8*, 531−554.
(33) Vecchiarelli, A. G.; Neuman, K. C.; Mizuuchi, K. A propagating ATPase gradient drives transport of surface-confined cellular cargo. *Proc. Natl. Acad. Sci. U.S.A.* **2014**, *111*, 4880.
(34) Sakai, T.; Takagi, H.; Muraki, Y.; Saito, M. Unique Directional Motility of Influenza C Virus Controlled by Its Filamentous Morphology and Short-Range Motions. *J. Virol.* **2018**, *92*, No. e01522.
(35) Ziebert, F.; Kulić, I. M. How Influenza's Spike Motor Works. *Phys. Rev. Lett.* **2021**, *126*, 218101.
(36) Sarkar, A.; LeVine, D. N.; Kuzmina, N.; Zhao, Y.; Wang, X. Cell Migration Driven by Self-Generated Integrin Ligand Gradient on Ligand-Labile Surfaces. *Curr. Biol.* **2020**, *30*, 4022−4032.
(37) Nakamura, A.; Okazaki, K.-i.; Furuta, T.; Sakurai, M.; Iino, R. Processive chitinase is Brownian monorail operated by fast catalysis after peeling rail from crystalline chitin. *Nat. Commun.* **2018**, *9*, 3814.
(38) Sarkar, S. K.; Marmer, B.; Goldberg, G.; Neuman, K. C. Single-Molecule Tracking of Collagenase on Native Type I Collagen Fibrils Reveals Degradation Mechanism. *Curr. Biol.* **2012**, *22*, 1047−1056.
(39) blanchard, A. T. Burnt bridge ratchet motor force scales linearly with polyvalency: a computational study. *Soft Matter* **2021**, *17*, 6056−6062.
(40) Korosec, C. S.; Forde, N. R. The lawnmower: an artificial protein-based burnt-bridge molecular motor. arXiv e-prints, **2021**. arXiv:2109.10293.
(41) Hu, L.; Vecchiarelli, A. G.; Mizuuchi, K.; Neuman, K. C.; Liu, J. Directed and persistent movement arises from mechanochemistry of the ParA/ParB system. *Proc. Natl. Acad. Sci. U.S.A.* **2015**, *112*, No. E7055.
(42) Korosec, C. S.; Jindal, L.; Schneider, M.; Calderon de la Barca, I.; Zuckermann, M. J.; Forde, N. R.; Emberly, E. Substrate stiffness tunes the dynamics of polyvalent rolling motors. *Soft Matter* **2021**, *17*, 1468−1479.
(43) Korosec, C. S.; Zuckermann, M. J.; Forde, N. R. Dimensionality-dependent crossover in motility of polyvalent burnt-bridges ratchets. *Phys. Rev. E* **2018**, *98*, 032114.
(44) Jindal, L.; Emberly, E. Operational Principles for the Dynamics of the In Vitro ParA-ParB System. *PLoS Comput. Biol.* **2015**, *11*, No. e1004651.
(45) Arredondo, D.; Stefanovic, D. Effect of polyvalency on tethered molecular walkers on independent one-dimensional tracks. *Phys. Rev. E* **2020**, *101*, 062101.
(46) Semenov, O.; Mohr, D.; Stefanovic, D. First-passage properties of molecular spiders. *Phys. Rev. E* **2013**, *88*, 012724.
(47) Semenov, O.; Olah, M. J.; Stefanovic, D. Mechanism of diffusive transport in molecular spider models. *Phys. Rev. E* **2011**, *83*, 021117.
(48) Chiara, L.; Andrea, G.; Annalisa, C.; Davide, B.; Manisha, S.; Ann, F.; S, T.; Giovanni, M. P. Towards Chemotactic Supramolecular Nanoparticles: From Autonomous Surface Motion Following Specific Chemical Gradients to Multivalency-Controlled Disassembly. *ACS nano* **2021**, *15*, 16149−16161.
(49) Hu, L.; Vecchiarelli, A. G.; Mizuuchi, K.; Neuman, K. C.; Liu, J. Brownian Ratchet Mechanism for Faithful Segregation of Low-Copy-Number Plasmids. *Biophys. J.* **2017**, *112*, 1489−1502.
(50) Hammer, D. A. Adhesive Dynamics. *J. Biomech. Eng.* **2014**, *136*, 021006−02100610.
(51) Paszek, M. J.; Boettiger, D.; Weaver, V. M.; Hammer, D. A. Integrin Clustering Is Driven by Mechanical Resistance from the Glycocalyx and the Substrate. *PLoS Comput. Biol.* **2009**, *5*, No. e1000604.
(52) Bidone, T. C.; Skeeters, A. V.; Oakes, P. W.; Voth, G. A. Multiscale model of integrin adhesion assembly. *PLoS Comput. Biol.* **2019**, *15*, No. e1007077.
(53) Anderson, N. R.; Lee, D.; Hammer, D. A. Adhesive dynamics simulations quantitatively predict effects of kindlin-3 deficiency on T-cell homing. *Integr. Biol.* **2019**, *11*, 293−300.
(54) Samii, L.; Linke, H.; Zuckermann, M. J.; Forde, N. R. Biased motion and molecular motor properties of bipedal spiders. *Phys. Rev. E* **2010**, *81*, 021106.
(55) Samii, L.; Blab, G. A.; Bromley, E. H. C.; Linke, H.; Curmi, P. M. G.; Zuckermann, M. J.; Forde, N. R. Time-dependent motor properties of multipedal molecular spiders. *Phys. Rev. E* **2011**, *84*, 031111.
(56) Olah, M. J.; Stefanovic, D. Superdiffusive transport by multivalent molecular walkers moving under load. *Phys. Rev. E* **2013**, *87*, 062713.
(57) Rank, M.; Reese, L.; Frey, E. Cooperative effects enhance the transport properties of molecular spider teams. *Phys. Rev. E* **2013**, *87*, 032706.
(58) Vahey, M. D.; Fletcher, D. A. Influenza A virus surface proteins are organized to help penetrate host mucus. *eLife* **2019**, *8*, No. e43764.
(59) Marko, J. F.; Siggia, E. D. Stretching DNA. *Macromolecules* **1995**, *28*, 8759−8770.
(60) Petrosyan, R. Improved approximations for some polymer extension models. *Rheol. Acta* **2017**, *56*, 21−26.
(61) Becker, N. B.; Rosa, A.; Everaers, R. The radial distribution function of worm-like chains. *Eur. Phys. J. E* **2010**, *32*, 53−69.
(62) Whitley, K. D.; Comstock, M. J.; Chemla, Y. R. Elasticity of the transition state for oligonucleotide hybridization. *Nucleic Acids Res.* **2017**, *45*, 547−555.
(63) Mosayebi, M.; Louis, A. A.; Doye, J. P. K.; Ouldridge, T. E. Force-Induced Rupture of a DNA Duplex: From Fundamentals to Force Sensors. *ACS Nano* **2015**, *9*, 11993−12003.
(64) Stone, H. A.; Stroock, A. D.; Ajdari, A. Engineering Flows in Small Devices: Microfluidics Toward a Lab-on-a-Chip. *Annu. Rev. Fluid Mech.* **2004**, *36*, 381−411.
(65) King, M. R.; Hammer, D. A. Multiparticle adhesive dynamics: Hydrodynamic recruitment of rolling leukocytes. *Proc. Natl. Acad. Sci. U.S.A.* **2001**, *98*, 14919.
(66) Trister, A. D.; Hammer, D. A. Role of gp120 Trimerization on HIV Binding Elucidated with Brownian Adhesive Dynamics. *Biophys. J.* **2008**, *95*, 40−53.
(67) PACE {P}artnership for an {A}dvanced {C}omputing {E}nvironment ({PACE}), 2017.

https://doi.org/10.1021/acs.jpcb.2c01897
J. Phys. Chem. B 2022, 126, 7495−7509